

Deep learning of thermodynamic laws from microscopic dynamics

Hiroto Kuroyanagi¹ and Tatsuro Yuge¹

¹*Department of Physics, Shizuoka University, Shizuoka 422-8529, Japan*

We numerically show that a deep neural network (DNN) can learn macroscopic thermodynamic laws purely from microscopic data. Using molecular dynamics simulations, we generate the data of snapshot images of gas particles undergoing adiabatic processes. We train a DNN to determine the temporal order of input image pairs. We observe that the trained network induces an order relation between states consistent with adiabatic accessibility, satisfying the axioms of thermodynamics. Furthermore, the internal representation learned by the DNN act as an entropy. These results suggest that machine learning can discover emergent physical laws that are valid at scales far larger than those of the underlying constituents—opening a pathway to data-driven discovery of macroscopic physics.

I. INTRODUCTION

In recent years, significant advances in machine learning (ML), particularly deep neural networks (DNNs) [1, 2], have led to many studies applying these methods to physics. One such area of studies is the discovery of physical laws from data using ML. Symbolic regressions have successfully rediscovered symbolic expressions of many physical laws from data [3–7]. ML-based modelings of dynamical equations have succeeded in predicting time evolution of systems from time-series data [8–11]. Also, several works have proposed ML algorithms that find hidden symmetries and conservation laws [12–15]. These approaches typically aim to discover laws that are valid at the same scale as the data—microscopic laws from microscopic data or macroscopic laws from macroscopic data. It remains to be elusive whether ML can discover physical laws emergent at macroscopic level from microscopic data though there are several studies on ML-based finding of appropriate latent variables whose dimension is significantly reduced compared with that of data [13, 16–19]. A typical example of emergent macroscopic laws is thermodynamics [20–23]. Given only the data of dynamics of microscopic elements, it is significantly difficult to find the laws of thermodynamics.

Another area of studies is ML-based analysis of thermodynamics and statistical mechanics. Earlier work [24] used Boltzmann machines to learn probability distribution of microscopic states from data of spin configurations generated by Monte Carlo simulation in equilibrium situations. In this line of research, supervised and unsupervised MLs are used to detect phase transitions from data of microscopic state in several systems [25–42]. In many of these studies, thermodynamic quantities like order parameters are explicitly extracted in latent variables or implicitly encoded in weights of neural networks. However, these studies do not pursue ML-based discovery of thermodynamic laws from microscopic data.

In this paper, we demonstrate that we can construct a DNN in which thermodynamics laws are encoded by training with data of microscopic elements. As microscopic data, we use images (extremely short videos) of particles generated by molecular dynamics (MD) simu-

lation of gas particles. The DNN is supervisedly trained with the microscopic data to classify which microscopic image corresponds to the later-time state. We numerically show that the classification of the trained DNN induces an order relation that satisfies the axioms of thermodynamics. Moreover, the representation of an input microscopic image extracted by the trained DNN corresponds to an entropy of the state.

A related work is Ref. [43], in which a binary classification between forward and backward trajectories is used to determine the arrow of time. The authors of Ref. [43] have shown that the entropy production is extracted in the representation of the optimal neural network. In their study the input is the whole trajectories of small systems (a single Brownian particle and few spins) in contact with a thermal bath and driven by an external agent, whereas the input of our study is an image at a certain time of a larger system of gas particles in an adiabatic process. Also, our demonstration is not only finding the entropy in the representation of the neural network but also automatic encoding of the axioms of thermodynamics.

II. BRIEF REVIEW OF THERMODYNAMICS

To clarify what would demonstrate that a DNN has learned thermodynamic laws, we briefly review the axiomatic framework of thermodynamics developed by Lieb and Yngvason [21] (see also Refs. [22, 23]).

We consider a thermodynamic system and its state space Γ consisting of macroscopic equilibrium states of the system. Composition of two states $X \in \Gamma_1$ and $Y \in \Gamma_2$ is denoted by (X, Y) . Scaling by factor λ of a state $X \in \Gamma$ is denoted by λX . The important concept in the framework is the adiabatic accessibility from X to Y —symbolically expressed by $X \prec Y$, which means that there exists an adiabatic process that transforms X to Y . We write $X \sim Y$ if $X \prec Y$ and $Y \prec X$. Also, we write $X \prec\prec Y$ if $X \prec Y$ but $Y \not\prec X$. We say X and Y are comparable if either $X \prec Y$ or $Y \prec X$ holds.

The framework assumes the following basic axioms [21]:

(A1) Reflectivity: $X \sim X$.

- (A2) Transitivity: $X \prec Y$ and $Y \prec Z$ implies $X \prec Z$.
- (A3) Consistency: $X \prec Y$ and $X' \prec Y'$ implies $(X, X') \prec (Y, Y')$.
- (A4) Scaling invariance: If $X \prec Y$, then $\lambda X \prec \lambda Y$ for all $\lambda > 0$.
- (A5) Splitting and recombination: For $0 < \lambda < 1$, $X \sim (\lambda X, (1 - \lambda)X)$.
- (A6) Stability: For two states X and Y , if $(X, \varepsilon_k Z_0) \prec (Y, \varepsilon_k Z_1)$ holds for a sequence of factors ε_k tending to zero and some Z_0, Z_1 , then $X \prec Y$.

It is also assumed that any two states in the same state space are comparable. This is called Comparison Hypothesis and is eventually derived from the above and additional axioms in Ref. [21].

From these axioms and CH, we can construct an essentially unique thermodynamic entropy S , which satisfies the monotonicity— $X \prec Y$ if and only if $S(X) \leq S(Y)$, extensivity— $S(\lambda X) = \lambda S(X)$, and additivity— $S(X, Y) = S(X) + S(Y)$.

In constructing the thermodynamic entropy S , Ref. [21] introduces a canonical entropy S_Γ for a state space Γ as

$$S_\Gamma(X|X_*, X_{**}) = \sup\{\lambda : ((1 - \lambda)X_*, \lambda X_{**}) \prec X\}, \quad (1)$$

where $X_*, X_{**} \in \Gamma$ are reference states that satisfy $X_* \prec X_{**}$. Change of reference states yields an affine transformation of canonical entropy: $S_\Gamma(X|X'_*, X'_{**}) = \alpha S_\Gamma(X|X_*, X_{**}) + \beta$. The canonical entropy satisfies the monotonicity when X and Y are in the same state space. It is shown that there exists a pair of reference states (and resulting α, β) for every state space, such that the canonical entropy can be regarded as the thermodynamic entropy, which satisfies the monotonicity, extensivity, and additivity [21].

Let us also introduce a useful conceptual tool: Lieb–Yngvason machine [23, 44]. It is a device that determines whether $X_0 \prec X_1$ holds or not, based on the order relation \prec satisfying (A1)–(A6). The operation of a Lieb–Yngvason machine is expressed by the following binary-valued function F_{LY} of two comparable states X_0, X_1 ,

$$F_{LY}(X_0, X_1) = \begin{cases} 1 & (X_0 \prec X_1) \\ 0 & (\text{otherwise}). \end{cases} \quad (2)$$

In terms of the Lieb–Yngvason machine, the canonical entropy $S_\Gamma(X|X_*, X_{**})$ in Eq. (1) is identified with λ at which the value of $f(\lambda) \equiv F_{LY}(((1 - \lambda)X_*, \lambda X_{**}), X)$ jumps from one to zero.

From the axiomatic thermodynamics, we specify our goal for demonstrating that a DNN can learn thermodynamic laws: Can we make a DNN machine that behaves like a Lieb–Yngvason machine by training it with microscopic data and without prior knowledge of thermodynamics?

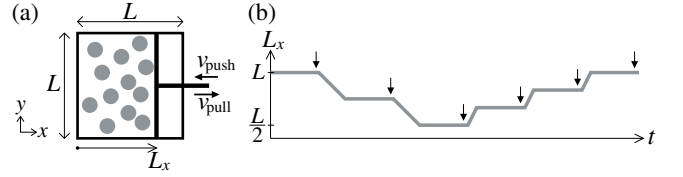


FIG. 1. (a) Schematic illustration of the MD simulation model. (b) An example of time profile of the piston position L_x for a single cycle. Five snapshots (an extremely short video) are taken at each of the times indicated by the down arrows.

III. METHODS

A. Preparation of data: MD simulation

We use MD simulation to prepare the dataset in this study. This is because we would like to demonstrate that a DNN can learn thermodynamics from microscopic physics and the training data should obey the microscopic laws (classical mechanics in this study). Moreover, since we would like to train a DNN without prior knowledge of thermodynamics and statistical mechanics, we do not use any thermostats or barostats in the simulation. In the same reason, we do not use Monte Carlo simulation in contrast to the previous studies [24–42] (Monte Carlo simulation samples data from canonical ensemble, so that it contains quantities specific to thermodynamics).

We consider a two-dimensional system of N particles in a thermally insulated container of size $L \times L$, as schematically depicted in Fig. 1(a). We have a piston on the right side of the container and can control its position L_x and speed $v_{\text{push/pull}}$, as shown in Fig. 1(b).

We assume a short-range repulsive interaction between the particles. Specifically, the interaction potential between the i th and j th particles (at the positions of \mathbf{r}_i and \mathbf{r}_j , respectively) is

$$\phi(\mathbf{r}_i, \mathbf{r}_j) = \begin{cases} \frac{1}{2} C_{\text{int}} (2R - r_{i,j})^2 & (r_{i,j} \leq 2R) \\ 0 & (r_{i,j} > 2R), \end{cases} \quad (3)$$

where the positive constant C_{int} represents the interaction strength, R is the radius of each particle, and $r_{i,j} = |\mathbf{r}_i - \mathbf{r}_j|$. We also assume that the repulsive interaction potential ϕ_{wall} between the particles and the container, or the piston, have functional forms similar to that of Eq. (3).

The initial positions of the particles are randomly arranged with the condition of no overlap. The initial velocities of the particles are sampled from the Maxwell distribution with temperature T_0 . In the simulation, we express physical quantities in units of energy $k_B T_0$, length R , and time $R\sqrt{m/k_B T_0}$, where m is the particle mass. We set $L = 300$ and $C_{\text{int}} = 10000$ in these units and $N = 500, 1000, 1500, 2000$ for individual simulation runs.

We adopt the velocity Verlet algorithm [45] for integrating the equations of motion in time t , where the time-step width is 0.001.

We control the piston as follows. Initially, we set it at $L_x = L$. After a while, we begin to push it at a constant speed v_{push} . When we move it a certain distance ΔL_{push} , we stop and hold it for a while. We repeat these push and stop periods until it reaches $L_x = L/2$. Then we reverse the direction by repeating pull and stop periods until it returns to $L_x = L$, where the speed of the piston is v_{pull} and the distance moved in a period is ΔL_{pull} . In a single run of the MD simulation, we repeat this cycle of $L_x = L \rightarrow L/2 \rightarrow L$ [Fig. 1(b)] three times. We refer to an entire sequence composed of these three cycles as a “process.” We note that a process is thermodynamically adiabatic because the container and piston are the potential walls and no thermostats are used. We also note that the density (packing fraction) $\eta = N\pi R^2/(LL_x)$ is smaller than 0.14 in our simulation, which implies that the system is in the dilute gas phase and far from the Alder-type transition point ($\eta \sim 0.7$) [46, 47].

We perform MD simulation for 448 processes. Each of the processes has a different set of values of $N \in \{500, 1000, 1500, 2000\}$, $v_{\text{push/pull}} \in \{0.1, 0.5\}$, and $\Delta L_{\text{push/pull}} \in \{150, 75, 50, 37.5, 30, 25, 18.75, 15, 10, 7.5\}$.

At around the end of each stop period in a process, we record the positions of the particles five times, with a time interval of $\Delta t = 1$ between each recording. At each recording time, we create a snapshot image of 1560×1560 pixels by drawing circles of radius R at the recorded positions and compress it to a 256×256 pixel image using the Lanczos filter. Every stop period, we thus obtain a series of five images, which composes an extremely short video and represents a microscopic state (positions and velocities of the particles) in an equilibrium situation. Hereafter, we refer to a single series of the five images simply as a “microscopic image” or “microscopic state.”

B. Neural network and supervised learning

As discussed at the end of Sec. II, our goal is to make a DNN machine that behaves like a Lieb–Yngvason machine with microscopic data and without prior knowledge of thermodynamics. To achieve this goal, we consider the following binary classification problem: Given a pair of microscopic images sampled from a single process in Sec. III A, which image corresponds to the later-time state? In this problem, each sample in the dataset consists of $(X_0, X_1; y)$, where the input variables X_0 and X_1 are two microscopic images and the target variable $y \in \{0, 1\}$ represents the image label of the later state (i.e., X_y is the later state) in the actual MD simulation.

Our neural network architecture for this problem is depicted in Fig. 2. It consists of two subnetworks (denoted by DNN-0 and DNN-1), which are convolutional neural networks sharing the parameters (weights and biases). DNN-0 (DNN-1) takes a microscopic image

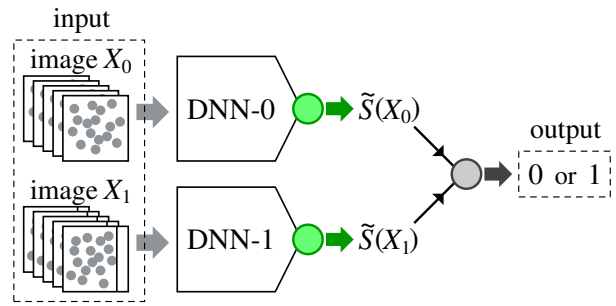


FIG. 2. Schematic illustration of the DNN model. The input is a pair of microscopic states X_0 and X_1 , each of which is an image having 256×256 pixels and five channels. The five channels correspond to the snapshots composing an extremely short video. Each of the two subnetworks DNN-0 and DNN-1 outputs a representation \tilde{S} of the input image. The two representations are fed forward to the sigmoid unit in the output layer of the whole network to compute the probability of X_1 being the later state. The output is the label of the predicted later state.

X_0 (X_1) as an input and outputs a single value of a representation $\tilde{S}(X_0)$ ($\tilde{S}(X_1)$) of the image, where the detailed structure of the subnetwork is shown in Table I. These representations are fed forward to the neuron in the output layer of the whole network. It computes the probability p that X_1 is the later state by $p = f_{\text{sigmoid}}(\tilde{S}(X_1) - \tilde{S}(X_0))$ and outputs 0 if $p < 1/2$ and 1 otherwise, where $f_{\text{sigmoid}}(x) = 1/(1 + e^{-x})$ is the logistic sigmoid function. We express the overall operation of this DNN architecture as $F_{\text{DNN}}(X_0, X_1)$, which is a binary-valued function of two states X_0, X_1 . We note that this type of a neural network composed of twin subnetworks is called siamese neural network [12, 48–51], which are used for measuring similarity between a pair of inputs.

We have thus constructed the DNN model F_{DNN} that has the inputs and output similar to those of the Lieb–Yngvason machine F_{LY} . We note that the inputs X_0, X_1 of F_{DNN} are microscopic states whereas those of F_{LY} are macroscopic states.

We train the DNN with the cross-entropy loss function and the Adam optimizer with a decreasing learning rate [1, 2]. Among the 448 processes in the MD simulation, 336 and 56 processes are used for training and validation, respectively, and the remaining 56 processes are used for test. To the training data we apply data augmentation consisting of image rotation (by angle $\pi/2$, π and $3\pi/2$), image flip (in the x- and y-directions), time-reverse of video, and their combinations. After training, we evaluate the performance of the DNN with the test dataset. The test loss is 0.1041 and the test accuracy is 0.9534. We use TensorFlow [52] to implement and train the DNN.

TABLE I. Structure of a subnetwork in the DNN model, which corresponds to DNN-0 or DNN-1 in Fig. 2. All convolutional layers have filters of size 2×2 with a stride of 2.

Layer	Hyperparameter	Activation
Convolutional	Output channels: 16	ReLU
Convolutional	Output channels: 32	ReLU
Convolutional	Output channels: 64	ReLU
Convolutional	Output channels: 64	ReLU
Convolutional	Output channels: 128	ReLU
Flatten	-	-
Dropout	Rate: 0.25	-
Dense	Output units: 128	ReLU
Dense	Output units: 64	ReLU
Dense	Output units: 1	Linear

IV. RESULTS

A. Axiomatic properties of the DNN

We now investigate whether the trained DNN machine have learned the thermodynamic laws. We define the order relation \prec_{DNN} induced by the machine: $X \prec_{\text{DNN}} Y$ if $F_{\text{DNN}}(X, Y) = 1$. In the following, using the test dataset, we demonstrate that \prec_{DNN} satisfies the axioms (A1)–(A6) within the numerical precision. This demonstration implies that the machine behaves like a Lieb–Yngvason machine. We note that, by definition, $X \prec_{\text{DNN}} Y$ if and only if $\tilde{S}(X) \leq \tilde{S}(Y)$. Also, we write $X \sim_{\text{DNN}} Y$ if both $X \prec_{\text{DNN}} Y$ and $Y \prec_{\text{DNN}} X$ hold.

Firstly, we consider the reflectivity (A1). By the definition of the DNN machine, it is obvious that $X \sim_{\text{DNN}} X$ holds. However, we note that \sim and \prec are the relations between macroscopic states whereas \sim_{DNN} and \prec_{DNN} are the ones between microscopic states. Therefore, to demonstrate (A1), we must examine whether $X \sim_{\text{DNN}} X'$ holds if X and X' are macroscopically equivalent. We also note that confirming $\tilde{S}(X) = \tilde{S}(X')$ with small error is sufficient to numerically demonstrate $X \sim_{\text{DNN}} X'$. To create a state X' macroscopically equivalent to X , we perform another MD simulation run of the same process as that of X , starting with a microscopically different but macroscopically equivalent initial state (with the same initial values of energy, volume and particle number). As seen in Fig. 3, $\tilde{S}(X) \simeq \tilde{S}(X')$ holds for most of the test data. In fact, the coefficient of determination R^2 of the plot in Fig. 3 is 0.9951, which is near to 1 and therefore numerically demonstrates (A1).

Secondly, we consider the transitivity (A2). This is obviously valid because $X \prec_{\text{DNN}} Y$ and $Y \prec_{\text{DNN}} Z$ imply $\tilde{S}(X) \leq \tilde{S}(Y) \leq \tilde{S}(Z)$ and thus $X \prec_{\text{DNN}} Z$.

Thirdly, we consider the consistency (A3). We create a compound state (X, X') as follows [Fig. 4(a)]: We take two states X and X' where the pistons are located at $L_x = L/2$, cut out the half of each of the two images where the particles are confined, and combine them to create a single image of (X, X') . We investigate

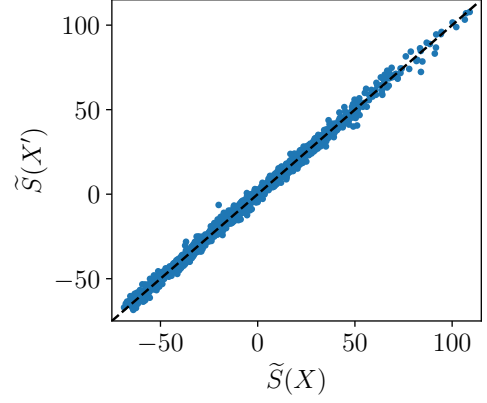


FIG. 3. Numerical demonstration of (A1). The representation \tilde{S} of a state X' macroscopically equivalent to X is plotted against $\tilde{S}(X)$. The dashed line shows $\tilde{S}(X') = \tilde{S}(X)$.

the prediction agreement rate, defined by $|D_{\text{A3}}^{\text{agree}}|/|D_{\text{A3}}|$, where $D_{\text{A3}} = \{(X, X', Y, Y') \mid X \prec_{\text{DNN}} Y, X' \prec_{\text{DNN}} Y', L_x(X) = L_x(X') = L_x(Y) = L_x(Y') = L/2\}$ and $D_{\text{A3}}^{\text{agree}} = \{(X, X', Y, Y') \in D_{\text{A3}} \mid (X, X') \prec_{\text{DNN}} (Y, Y')\}$ in the test dataset, and $|D|$ represents the number of data in a dataset D . We find that the prediction agreement rate is 0.9995. That is, if $X \prec_{\text{DNN}} X'$ and $Y \prec_{\text{DNN}} Y'$, this DNN model can predict $(X, X') \prec_{\text{DNN}} (Y, Y')$ with the accuracy of 99.95%, which demonstrates (A3).

Fourthly, we consider the scaling invariance (A4). To create a scaled state λX , we mask the $(1 - \lambda)$ fraction of either the bottom or right region of the microscopic image X [Fig. 4(b)], where we use five different values of λ ($= 0.5, 0.6, 0.7, 0.8, 0.9$). We investigate the prediction agreement rate, $(1/5) \sum_{\lambda} |D_{\text{A4}}^{\text{agree}}(\lambda)|/|D_{\text{A4}}|$ with $D_{\text{A4}} = \{(X, Y) \mid X \prec_{\text{DNN}} Y\}$ and $D_{\text{A4}}^{\text{agree}}(\lambda) = \{(X, Y) \in D_{\text{A4}} \mid \lambda X \prec_{\text{DNN}} \lambda Y\}$ in the test dataset. We find that the prediction agreement rate is 0.9417, which demonstrates (A4) with the accuracy of 94.17%. The prediction agreement rate of (A4) is lower than that of (A3). This is possibly because the number of particles $N(\lambda X)$ in the scaled state (created by masking) is not exactly the same as $\lambda N(X)$ and the deviation $N(\lambda X) - \lambda N(X)$ fluctuates sample by sample.

Fifthly, we consider the splitting and recombination (A5). The method of creating a split state $X_{\text{split}} = (\lambda X, (1 - \lambda)X)$ from a state X is as follows. We insert a wall that is parallel to either the x-direction (at $L_y^{\text{wall}} = \lambda L$) or the y-direction (at $L_x^{\text{wall}} = \lambda L_x$) into the state X . We remove the particles that are located in the region of the wall to avoid extremely large force between the wall and the particles. We then perform the MD simulation from this new state for a short time with the wall and piston fixed to obtain a split state. We also create a recombined state X_{recomb} from a split state $(\lambda X, (1 - \lambda)X)$ by removing the wall and performing the MD simulation for a short time. We investigate the representation \tilde{S} of the original state X and the split state X_{split} and the recombined state X_{recomb} . As shown in

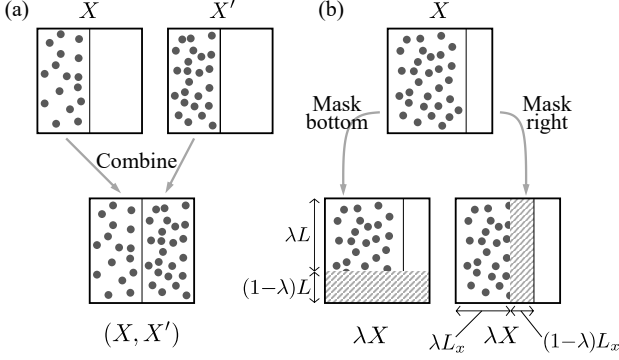


FIG. 4. (a) Illustration of creating a compound state (X, X') . The images of two states, X and X' , where the pistons are at $L_x = L/2$ are combined into a single image of (X, X') . (b) Illustration of creating a scaled state λX . Either the bottom or right part (shaded) in the image of a state X is masked. In the actual data, the masked region is filled with zero.

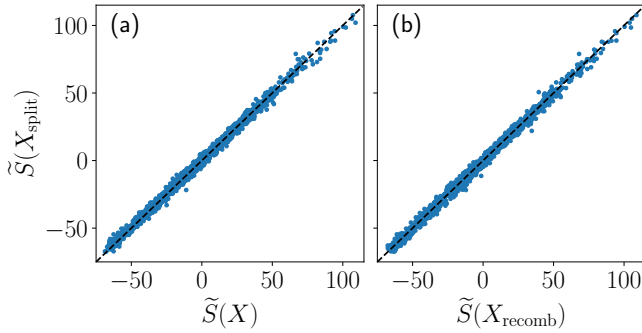


FIG. 5. Demonstration of (A5). The representation \tilde{S} of a split state X_{split} is plotted against $\tilde{S}(X)$ in (a) and against $\tilde{S}(X_{\text{recomb}})$ in (b). The dashed lines show $\tilde{S}(X_{\text{split}}) = \tilde{S}(X)$ in (a) and $\tilde{S}(X_{\text{split}}) = \tilde{S}(X_{\text{recomb}})$ in (b), respectively.

Fig. 5, $\tilde{S}(X_{\text{split}})$ is close to both $\tilde{S}(X)$ and $\tilde{S}(X_{\text{recomb}})$ for most of the test data. The determination coefficients R^2 of the plots in Figs. 5(a) and (b) are 0.9949 and 0.9946, respectively, which demonstrates (A5).

Finally, we consider the stability (A6). With the help of Comparison Hypothesis, when we restrict X and Y to belong to the same state space Γ , the statement of (A6) is reduced to the following: If $X \prec_{\text{DNN}} Y$, then for sufficiently small $\varepsilon > 0$, $(X, \varepsilon Z_1) \prec_{\text{DNN}} (Y, \varepsilon Z_2)$ holds for any states Z_1 and Z_2 . That is, small dusts, εZ_1 and εZ_2 , do not break the order relation between X and Y . We here demonstrate this reduced statement. We create a state $(X, \varepsilon Z)$ from X and Z by taking an ε -fraction of Z and embedding it into X (inset of Fig. 6). We investigate the prediction agreement rate, $|D_{A6}^{\text{agree}}|/|D_{A6}|$, where $D_{A6} = \{(X, Y) \mid X \prec_{\text{DNN}} Y\}$ and $D_{A6}^{\text{agree}} = \{(X, Y) \in D_{A6} \mid (X, \varepsilon Z_1) \prec_{\text{DNN}} (Y, \varepsilon Z_2)\}$ with a fixed pair states, Z_1 and Z_2 . Figure 6 shows that the prediction agreement rate approaches 1 as ε decreases for a pair of Z_1 and Z_2 . We observe similar behaviors of

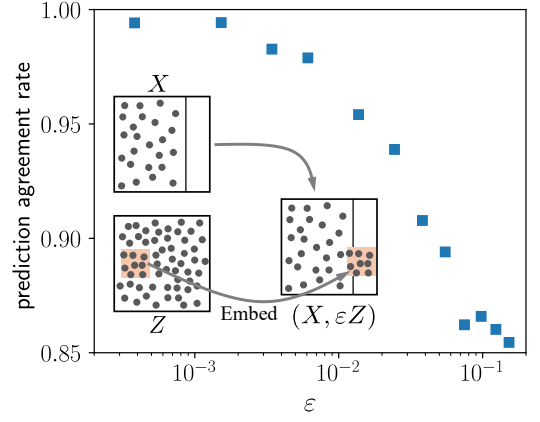


FIG. 6. Demonstration of (A6). The prediction agreement rate $|D_{A6}^{\text{agree}}|/|D_{A6}|$ is plotted against the relative size ε of a dust state εZ . The inset shows how to create a state of $(X, \varepsilon Z)$ from X and Z .

the prediction agreement rate for several other pairs (not shown), which demonstrates (A6).

B. Representation \tilde{S} as an entropy

In the previous subsection, we have shown that the DNN-induced order relation \prec_{DNN} satisfies the axioms (A1)–(A6) within the numerical precision. We next demonstrate that the representation $\tilde{S}(X)$ of the trained DNN machine can be interpreted as a canonical entropy. This demonstration justifies that \prec_{DNN} is actually identified with the order relation \prec of the adiabatic accessibility because \prec_{DNN} is determined based on $\tilde{S}(X_0)$ and $\tilde{S}(X_1)$.

To demonstrate this, we numerically compare \tilde{S} for simple (non-compound) system of each fixed N with the entropy of the van der Waals gas. As described in Sec. III A, the system in the MD simulation is a two-dimensional gas of particles that interact only repulsively with each other. Therefore, it is expected that its thermodynamic property is well described by the two-dimensional monatomic van der Waals gas without attractive interaction. The thermodynamic entropy $S_{\text{vdW}}(U, V, N)$ of the van der Waals gas of energy U , volume V , and number of particles N reads [20]:

$$\begin{aligned} S_{\text{vdW}}(U, V, N) &= Nk_B \log \left[\left(u + \frac{a}{v} \right)^c (v - b) \right] + Ns_0 \\ &= Nk_B \log [u(v - b)] + Ns_0, \end{aligned} \quad (4)$$

where $u = U/N$, $v = V/N$, and s_0 is a constant. In the second line, we have used $a = 0$ (because of no attractive interaction) and $c = 1$ (because of two-dimensional monatomic gas). The constant b represents the excluded volume per particle due to the repulsive interaction. Since the sufficiently large interaction strength

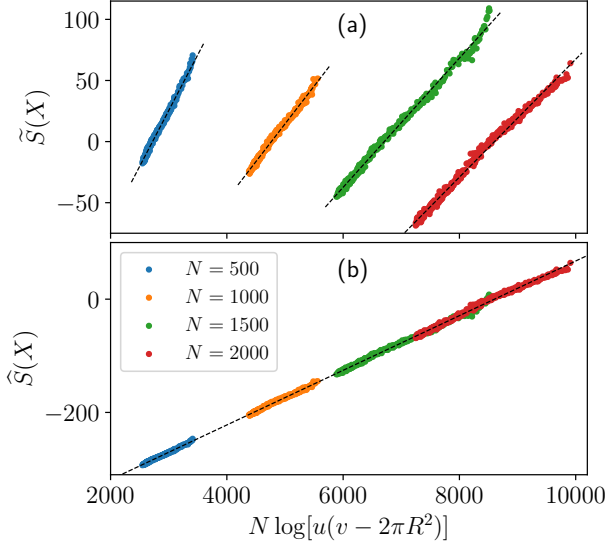


FIG. 7. Parametric plots of (a) the original representation $\tilde{S}(X)$ and (b) an appropriately affine transformed representation $\hat{S}(X)$ against $N \log[u(X)\{v(X) - 2\pi R^2\}]$ for $N = 500, 1000, 1500, 2000$. The dashed lines are the fitted lines that are linearly dependent on $N \log[u\{v - 2\pi R^2\}]$.

C_{int} is used in the MD simulation, it is reasonable to set $b = 2\pi R^2$.

In Fig. 7(a), we plot $\tilde{S}(X)$ against $N \log[u(X)\{v(X) - 2\pi R^2\}]$ for each of $N = 500, 1000, 1500, 2000$, where $u(X) = U(X)/N$ and $v(X) = V(X)/N$ with energy $U(X)$ and volume $V(X) = LL_x(X)$ of X , respectively. We observe that $\tilde{S}(X)$ is linearly dependent on $N \log[u(X)\{v(X) - 2\pi R^2\}]$ for each N . This implies that, for each N , \tilde{S} is a function of only the two macroscopic variables, u and v , and it is an affine transformation of S_{vdW} . Therefore, we can interpret $\tilde{S}(X)$ as a canonical entropy $S_{\Gamma_N}(X|X_*^{(N)}, X_{**}^{(N)})$ for each N , where Γ_N is the state space for the system of N particles and $X_*^{(N)}$ and $X_{**}^{(N)}$ are a pair of reference states in Γ_N .

Therefore, we can construct a thermodynamic entropy by an appropriate affine transformation $\hat{S}(X) = \alpha_N \tilde{S}(X) + \beta_N$. We show an example of the transformation in Fig. 7(b), where $\hat{S}(X) \propto S_{\text{vdW}}(U, V, N)$ [Eq.(4)] with $s_0 = 0$.

Furthermore, we investigate the monotonicity, extensivity and additivity of \tilde{S} . The monotonicity is valid if the order relation induced by the trained DNN satisfies (A1)–(A6), because the DNN model is written as $F_{\text{DNN}}(X_0, X_1) = \Theta(\tilde{S}(X_0) - \tilde{S}(X_1))$ with the step function $\Theta(x)$. We demonstrate the extensivity and additivity as follows. We create a compound state $(\lambda X, (1 - \lambda)Y)$ of two scaled states λX and $(1 - \lambda)Y$ in a similar way to that in Fig. 4 with $\lambda = 0.2, 0.3, \dots, 0.8$. In Fig. 8, we compare $\tilde{S}(\lambda X, (1 - \lambda)Y)$ with $\lambda \tilde{S}(X) + (1 - \lambda)\tilde{S}(Y)$, where X and Y have the same number of particles. We observe that $\tilde{S}(\lambda X, (1 - \lambda)Y)$ is almost linearly dependent

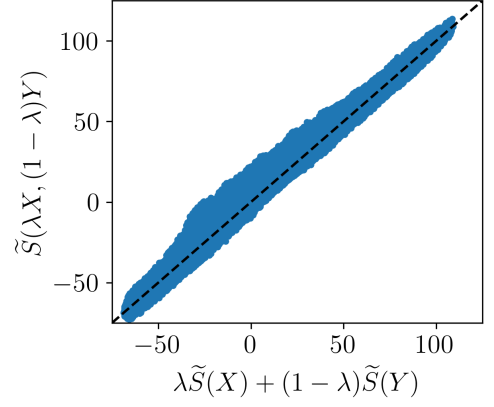


FIG. 8. Representation \tilde{S} of a compound state $(\lambda X, (1 - \lambda)Y)$ plotted against the sum of the scaled representations, $\lambda \tilde{S}(X) + (1 - \lambda)\tilde{S}(Y)$. The dashed line shows $\tilde{S}(\lambda X, (1 - \lambda)Y) = \lambda \tilde{S}(X) + (1 - \lambda)\tilde{S}(Y)$.

on $\lambda \tilde{S}(X) + (1 - \lambda)\tilde{S}(Y)$. The coefficient of determination R^2 of the plot is 0.9766, which illustrates that \tilde{S} is an extensive and additive quantity. Compared with the results for (A1) (Fig. 3) and (A5) (Fig. 5), the deviation $\tilde{S}(\lambda X, (1 - \lambda)Y) - [\lambda \tilde{S}(X) + (1 - \lambda)\tilde{S}(Y)]$ is larger and the coefficient of determination R^2 is smaller. This would be due to the same reason as that of the lower prediction agreement rate of (A4).

V. SUMMARY

In this study, we demonstrated that a DNN machine can behave as a Lieb–Yngvason machine—which is equipped with the order relation satisfying the axioms of thermodynamics—through the training with microscopic data of gas particles and without prior knowledge of thermodynamics. The order relation is determined by the representation of the microscopic image extracted by the trained DNN, and it is interpreted as a canonical entropy of the state.

In our demonstration, we used a gas system with short-range repulsive interactions. To establish the generality of our results, further investigations on a wider class of systems are necessary. Possible directions include a system of Lennard–Jones particles [53], which incorporate attractive interactions, and anharmonic lattice models [54]. Extending the analysis to quantum systems, beyond the classical regime considered here, is also an important future challenge.

Moreover, our study focused on densities well below the threshold for the Alder-type phase transition. It would be valuable to examine systems that exhibit phase transitions or phase coexistence.

Another important direction is to move beyond equilibrium and explore nonequilibrium settings. Whether macroscopic theories such as nonequilibrium thermody-

namics [55] or hydrodynamics can emerge from microscopic data remains an intriguing question.

Our results showed that entropy emerges in the representation of the DNN corresponding to an input of a microscopic state. This suggests that the DNN performs a certain form of statistical mechanics. However, un-

like the Boltzmann principle, it does not involve counting over all microscopic states since the input is a single microscopic state. This raises the possibility of a novel statistical mechanical framework. Exploring this direction may provide new insights into the foundations of statistical mechanics.

-
- [1] I. Goodfellow, Y. Bengio, and A. Courville, *Deep Learning* (MIT Press, Cambridge, MA, 2016).
 - [2] C. M. Bishop and H. Bishop, *Deep Learning - Foundations and Concepts* (Springer, Cham, Switzerland, 2024).
 - [3] S.-M. Udrescu and M. Tegmark, AI Feynman: A physics-inspired method for symbolic regression, *Sci. Adv.* **6**, eaay2631 (2020).
 - [4] S.-M. Udrescu, A. Tan, J. Feng, O. Neto, T. Wu, and M. Tegmark, AI Feynman 2.0: Pareto-optimal symbolic regression exploiting graph modularity, *Advances in Neural Information Processing Systems* **33**, 4860 (2020).
 - [5] L. S. Keren, A. Liberzon, and T. Lazebnik, A computational framework for physics-informed symbolic regression with straightforward integration of domain knowledge, *Sci. Rep.* **13**, 1249 (2023).
 - [6] C. Cornelio, S. Dash, V. Austel, T. R. Josephson, J. Goncalves, K. L. Clarkson, N. Megiddo, B. El Khadir, and L. Horesh, Combining data and theory for derivable scientific discovery with AI-Descartes, *Nat. Commun.* **14**, 1777 (2023).
 - [7] N. Makke and S. Chawla, Interpretable scientific discovery with symbolic regression: a review, *Artificial Intelligence Review* **57**, 2 (2024).
 - [8] S. Greydanus, M. Dzamba, and J. Yosinski, Hamiltonian neural networks, *Advances in neural information processing systems* **32** (2019).
 - [9] A. Choudhary, J. F. Lindner, E. G. Holliday, S. T. Miller, S. Sinha, and W. L. Ditto, Physics-enhanced neural networks learn order and chaos, *Physical Review E* **101**, 062207 (2020).
 - [10] M. Cranmer, S. Greydanus, S. Hoyer, P. Battaglia, D. Spergel, and S. Ho, Lagrangian neural networks, *arXiv preprint arXiv:2003.04630* (2020).
 - [11] C.-D. Han, B. Glaz, M. Haile, and Y.-C. Lai, Adaptable hamiltonian neural networks, *Physical Review Research* **3**, 023156 (2021).
 - [12] S. J. Wetzel, R. G. Melko, J. Scott, M. Panju, and V. Ganesh, Discovering symmetry invariants and conserved quantities by interpreting siamese neural networks, *Physical Review Research* **2**, 033499 (2020).
 - [13] Y.-i. Mototake, Interpretable conservation law estimation by deriving the symmetries of dynamics from trained deep neural networks, *Physical Review E* **103**, 033303 (2021).
 - [14] Z. Liu and M. Tegmark, Machine learning conservation laws from trajectories, *Phys. Rev. Lett.* **126**, 180604 (2021).
 - [15] Z. Liu and M. Tegmark, Machine learning hidden symmetries, *Phys. Rev. Lett.* **128**, 180201 (2022).
 - [16] K. Champion, B. Lusch, J. N. Kutz, and S. L. Brunton, Data-driven discovery of coordinates and governing equations, *Proceedings of the National Academy of Sciences* **116**, 22445 (2019).
 - [17] R. Iten, T. Metger, H. Wilming, L. Del Rio, and R. Renner, Discovering physical concepts with neural networks, *Phys. Rev. Lett.* **124**, 010508 (2020).
 - [18] S.-M. Udrescu and M. Tegmark, Symbolic pregression: Discovering physical laws from distorted video, *Physical Review E* **103**, 043307 (2021).
 - [19] B. Chen, K. Huang, S. Raghupathi, I. Chandratreya, Q. Du, and H. Lipson, Automated discovery of fundamental variables hidden in experimental data, *Nature Computational Science* **2**, 433 (2022).
 - [20] H. B. Callen, *Thermodynamics and an Introduction to Thermostatistics*, 2nd ed. (Wiley, New York, 1985).
 - [21] E. H. Lieb and J. Yngvason, The physics and mathematics of the second law of thermodynamics, *Physics Reports* **310**, 1 (1999).
 - [22] E. H. Lieb and J. Yngvason, A guide to entropy and the second law of thermodynamics, *Notices of the AMS* **45**, 571 (1998).
 - [23] A. Thess, *The entropy principle* (Springer Berlin, Heidelberg, 2011).
 - [24] G. Torlai and R. G. Melko, Learning thermodynamics with Boltzmann machines, *Phys. Rev. B* **94**, 165134 (2016).
 - [25] L. Wang, Discovering phase transitions with unsupervised learning, *Phys. Rev. B* **94**, 195105 (2016).
 - [26] T. Ohtsuki and T. Ohtsuki, Deep learning the quantum phase transitions in random two-dimensional electron systems, *J. Phys. Soc. Jpn.* **85**, 123706 (2016).
 - [27] J. Carrasquilla and R. G. Melko, Machine learning phases of matter, *Nature Physics* **13**, 431 (2017).
 - [28] P. Broecker, J. Carrasquilla, R. G. Melko, and S. Trebst, Machine learning quantum phases of matter beyond the fermion sign problem, *Scientific reports* **7**, 8823 (2017).
 - [29] A. Tanaka and A. Tomiya, Detection of phase transition via convolutional neural networks, *J. Phys. Soc. Jpn.* **86**, 063001 (2017).
 - [30] S. J. Wetzel, Unsupervised learning of phase transitions: From principal component analysis to variational autoencoders, *Physical Review E* **96**, 022140 (2017).
 - [31] S. J. Wetzel and M. Scherzer, Machine learning of explicit order parameters: From the ising model to su(2) lattice gauge theory, *Phys. Rev. B* **96**, 184410 (2017).
 - [32] K. Ch'ng, N. Vazquez, and E. Khatami, Unsupervised machine learning account of magnetic transitions in the hubbard model, *Physical Review E* **97**, 013306 (2018).
 - [33] S. Iso, S. Shiba, and S. Yokoo, Scale-invariant feature extraction of neural network and renormalization group flow, *Physical review E* **97**, 053304 (2018).
 - [34] A. Canabarro, F. F. Fanchini, A. L. Malvezzi, R. Pereira, and R. Chaves, Unveiling phase transitions with machine learning, *Phys. Rev. B* **100**, 045129 (2019).
 - [35] X.-Y. Dong, F. Pollmann, and X.-F. Zhang, Machine learning of quantum phase transitions, *Physical Review*

- B **99**, 121104 (2019).
- [36] W. Zhang, J. Liu, and T.-C. Wei, Machine learning of phase transitions in the percolation and XY models, *Physical Review E* **99**, 032142 (2019).
 - [37] K.-I. Aoki, T. Fujita, and T. Kobayashi, Logical reasoning for revealing the critical temperature through deep learning of configuration ensemble of statistical systems, *J. Phys. Soc. Jpn.* **88**, 054002 (2019).
 - [38] K. Kashiwa, Y. Kikuchi, and A. Tomiya, Phase transition encoded in neural network, *Progress of Theoretical and Experimental Physics* **2019**, 083A04 (2019).
 - [39] S. S. Funai and D. Giataganas, Thermodynamics and feature extraction by machine learning, *Physical Review Research* **2**, 033415 (2020).
 - [40] Y. Miyajima and M. Mochizuki, Machine-learning detection of the Berezinskii-Kosterlitz-Thouless transition and the second-order phase transition in XXZ models, *Phys. Rev. B* **107**, 134420 (2023).
 - [41] D. Bayo, B. Çivitcioglu, J. J. Webb, A. Honecker, and R. A. Römer, Machine learning of phases and structures for model systems in physics, *Journal of the Physical Society of Japan* **94**, 031002 (2025).
 - [42] M. Mochizuki and Y. Miyajima, Machine-learning detection of the berezinskii-kosterlitz-thouless transitions, *journal of the physical society of japan* **94**, 031003 (2025).
 - [43] A. Seif, M. Hafezi, and C. Jarzynski, Machine learning the thermodynamic arrow of time, *Nat. Phys.* **17**, 105 (2021).
 - [44] A. Thess, Was ist entropie? eine antwort für unzufriedene, *Forschung im Ingenieurwesen* **72**, 11 (2008).
 - [45] W. C. Swope, H. C. Andersen, P. H. Berens, and K. R. Wilson, A computer simulation method for the calculation of equilibrium constants for the formation of physical clusters of molecules: Application to small water clusters, *The Journal of chemical physics* **76**, 637 (1982).
 - [46] B. J. Alder and T. E. Wainwright, Phase transition in elastic disks, *Phys. Rev.* **127**, 359 (1962).
 - [47] M. Engel, J. A. Anderson, S. C. Glotzer, M. Isobe, E. P. Bernard, and W. Krauth, Hard-disk equation of state: First-order liquid-hexatic transition in two dimensions with three simulation methods, *Phys. Rev. E* **87**, 042134 (2013).
 - [48] J. Bromley, I. Guyon, Y. LeCun, E. Säckinger, and R. Shah, Signature verification using a” siamese” time delay neural network, *Advances in neural information processing systems* **6** (1993).
 - [49] S. Chopra, R. Hadsell, and Y. LeCun, Learning a similarity metric discriminatively, with application to face verification, in *2005 IEEE computer society conference on computer vision and pattern recognition (CVPR’05)*, Vol. 1 (IEEE, 2005) pp. 539–546.
 - [50] L. Bertinetto, J. Valmadre, J. F. Henriques, A. Vedaldi, and P. H. Torr, Fully-convolutional siamese networks for object tracking, in *Computer vision–ECCV 2016 workshops: Amsterdam, the Netherlands, October 8–10 and 15–16, 2016, proceedings, part II 14* (Springer, 2016) pp. 850–865.
 - [51] Y. Li, C. P. Chen, and T. Zhang, A survey on siamese network: Methodologies, applications, and opportunities, *IEEE Transactions on artificial intelligence* **3**, 994 (2022).
 - [52] M. Abadi, A. Agarwal, P. Barham, E. Brevdo, Z. Chen, C. Citro, G. S. Corrado, A. Davis, J. Dean, M. Devin, S. Ghemawat, I. Goodfellow, A. Harp, G. Irving, M. Isard, Y. Jia, R. Jozefowicz, L. Kaiser, M. Kudlur, J. Levenberg, D. Mané, R. Monga, S. Moore, D. Murray, C. Olah, M. Schuster, J. Shlens, B. Steiner, I. Sutskever, K. Talwar, P. Tucker, V. Vanhoucke, V. Vasudevan, F. Viégas, O. Vinyals, P. Warden, M. Wattenberg, M. Wicke, Y. Yu, and X. Zheng, *TensorFlow: Large-scale machine learning on heterogeneous systems* (2015).
 - [53] H. Watanabe, N. Ito, and C.-K. Hu, Phase diagram and universality of the lennard-jones gas-liquid system, *The Journal of Chemical Physics* **136**, 204102 (2012).
 - [54] K. Saito and A. Dhar, Heat conduction in a three dimensional anharmonic crystal, *Phys. Rev. Lett.* **104**, 040601 (2010).
 - [55] E. H. Lieb and J. Yngvason, The entropy concept for non-equilibrium states, *Proceedings of the Royal Society A: Mathematical, Physical and Engineering Sciences* **469**, 20130408 (2013).